Nanoscale

PAPER

View Article Online
View Journal | View Issue

Cite this: *Nanoscale*, 2026, **18**, 8093

Emissive perovskite quantum wires in robust nanocontainers: $CsPbX_3$ confined inside boron nitride nanotubes

Bea Botka, *[a] Erzsébet Dodony, [b] Gergely Németh, [a,c] Michael Stratton, [a] Ildikó Harsányi, [a] János Mózer, [a,d] Éva Kováts, [a] Ferenc Borondics [c] and Katalin Kamarás [a,b]

Received 11th December 2025,
Accepted 1st March 2026

DOI: 10.1039/d5nr05217c

rsc.li/nanoscale

Light emissive nanostructures were prepared from boron nitride nanotubes (BNNTs) filled with inorganic lead halide perovskites, $CsPbBr_3$ and $CsPbI_3$. These one-dimensional nanocontainers provide a platform for facile synthesis of high aspect ratio perovskite quantum wires having color-tunable, highly polarized emission. BNNTs form a flexible and robust protective shell around individual nanowires that mitigates degradation during post-processing for practical applications, while allowing the exploitation of the emission of the perovskite nanowires. The wire diameter can be tuned by choosing appropriate BNNT hosts, giving easy access to well-defined nanowires across the strongly quantum-confined diameter range. The individual encapsulated quantum wires can be used as building blocks for nanoscale photonic devices and to create large-scale flexible assemblies.

Metal halide perovskites have emerged as a novel class of materials for optoelectronic applications including photovoltaics, light-emitting diodes, photodetectors, and lasers. Amongst their notable properties are high photoluminescence (PL) quantum yield, a tunable bandgap, a large absorption coefficient, low lasing threshold, and high structural and dimensional tunability.[1–3] In their one-dimensional nanowire form, the two confined dimensions can give access to unique physical properties compared to their bulk counterparts. The non-confined third dimension can direct the transport of quantum particles and facilitate interfacing, making them interesting candidates for advanced solid-state devices.[3–10] However, synthesis of perovskite nanowires with well-controlled diameters and high aspect ratios is challenging, especially within the strongly quantum-confined size range, corresponding to a wire diameter of a few unit cells. In our discussion we refer to one-dimensional objects having a diameter in the nanometer size range as nanowires. The term quantum wire is used only for those nanowires that have a diameter in the intermediate or strongly quantum-confined size range, which is close to or below the natural delocalization length of the excitons in bulk perovskites. This is estimated to be 7 and 12 nm for $CsPbBr_3$ and $CsPbI_3$, respectively.[11]

Free-standing perovskite nanowires are typically synthesized by colloidal methods.[12–15] The rapid growth requires very precise control of the experimental conditions, leading to challenges in controlling the size and morphology of the resulting crystals. Furthermore, free-standing nanowires have severe stability issues, which hinder their use in practical applications. In solution, loss or deterioration of the surfactant layer or capping ligands surrounding the wires results in ripening and a diameter increase. Also, once removed from their solution, in air they typically deteriorate rapidly.[16–18]

In contrast, template-assisted growth can significantly simplify the synthesis and the encapsulation of the wires can offer protection from environmental stressors. Various porous matrices, such as mesoporous silica and titania, zeolites and metal organic frameworks, have been explored for confined growth of perovskite nanoparticles.[19–21] Anodized aluminum oxide and mesoporous silica are suitable templates for nanowires as well owing to their well-aligned cylindrical nanopore system.[8,22–26] Wire thicknesses down to 2.9 nm have been achieved using porous alumina membranes, although the efficiency of the pore filling is low at this scale.[24] The typical nanowire aspect ratios achieved in these hosts were between 10 and 30. Additionally, these are bulk composite systems, and the individual perovskite entities cannot be separated from each other for independent use, which limits both the analysis and the range of applications. Individually processable encapsulated perovskite nanowires are still scarce in the literature.

[a]*Institute for Solid State Physics and Optics, HUN-REN Wigner Research Centre for Physics, Budapest, 1121, Hungary. E-mail: botka.bea@wigner.hun-ren.hu*
[b]*Institute for Technical Physics and Materials Science, HUN-REN Centre for Energy Research, Budapest, 1121, Hungary*
[c]*SOLEIL Synchrotron, Saint Aubin, 91190, France*
[d]*Faculty of Natural Sciences, Budapest University of Technology and Economics, Hungary*

Recently bottlebrush block copolymers were shown to be suitable hosts to allow template-confined synthesis of individual, thin perovskite nanowires.[27] Precise control of the size and the diameter reaching the quantum-confined regime can be achieved by this method. The aspect ratios demonstrated were similar to those achieved in porous alumina. Although this method is suitable for synthesis of individual quantum wires, it lacks the protective function necessary during the postprocessing steps and for practical applications. Ideally, a robust and modifiable container is needed, such as boron nitride or carbon nanotubes, which have excellent mechanical and thermal stability.

Synthesis of perovskite quantum wires down to single unit cell thicknesses was recently demonstrated in carbon nanotubes.[28,29] The nanotube shell provides protection from the environment and allows synthesis of ultrahigh (300–600) aspect ratio quantum wires, and high entropy perovskite structures can also be synthesized due to the strong confinement effects,[29] although the emission of the perovskite is quenched because of the small bandgap of the host. Single-walled carbon nanotube-$CsPbBr_3$ ($CsPbBr_3$@SWNCT) heterostructures were used in field-effect transistors providing stable n-type doping to the carbon nanotubes and creating junctions with editable photoresponse.[7,30] A high-performance stable direct X-ray detector was constructed using Cs_3MCl_6@SWCNT.[29]

Boron nitride nanotubes, while being structurally analogous to their carbon counterparts, have very different electrical properties, which opens the avenue for new exciting potential applications compared to their carbon counterparts. Boron nitride nanotubes are optically transparent in the whole visible range, and because they possess a significantly larger bandgap than SWCNTs, the emission of the guest species is not quenched due to energy transfer, unlike in typical heterojunctions formed in SWCNT-hosted systems.[31] BNNTs were shown to be suitable hosts for aligned supramolecular assemblies and confined synthesis of various nanoribbons.[32–36] As boron nitride sheets are impermeable for solvents and gases, they are commonly used in optical experiments as transparent protective layers.[37] BNNTs provide an efficient protective barrier between the guest species and the environment, which can prevent chemical degradation and photobleaching of encapsulated luminophores and also reduce the toxicity in biological applications.[33]

Here, we report the preparation of emissive nanostructures consisting of high aspect ratio, few unit cell thick perovskite quantum wires encapsulated in BNNTs with a high filling ratio and explore the optical properties and stability of these nanostructures. The diameter of the host nanotube can precisely control the structure and therefore the bandgap of the guest inorganic crystal, and the strong confinement can lead to various surface termination patterns.[28] These one-dimensional perovskite quantum wires possess a linearly polarized and tunable PL, in addition to a significantly improved resistance to ambient environment. Encapsulation inside the robust but flexible BNNT shell enables easy post-processing. These individually protected quantum wires provide an excellent platform to explore the changes of the optical properties due to confinement effects and related structural changes. Additionally, they can form ideal building blocks for nanoscale photonic devices or large-scale flexible assemblies.

Experimental

Chemicals

High purity, open-ended boron nitride nanotubes synthesized by the high temperature/high pressure (HTP) method were supplied by BNNT LLC. Perovskite precursors (anhydrous CsI, CsBr, PbI_2, $PbBr_2$) were obtained from Sigma Aldrich and solvents (*N*,*N*-dimethyl formamide, toluene) from VWR International. Precursors used for the reactions were at least 99.999% trace metal basis.

Quantum wire synthesis

Perovskite quantum wires were grown using high-temperature solid-state synthesis inside boron nitride nanotubes; the method was adapted from ref. 28. First, the perovskites were prepared by mixing the precursors in an agate mortar in stoichiometric quantities inside an argon-filled glovebox. To produce $CsPbBr_3$ the precursors were annealed for 5 hours at 480 °C in a tube furnace inside a closed quartz tube sealed under vacuum. $CsPbI_3$ was prepared at 600 °C followed by 480 °C annealing for 5 hours. Heating and cooling rates of 2 and 1 °C per minute were used. Raman and photoluminescence spectroscopy methods were performed to characterize the resulting perovskite crystals (Fig. S4). In the above reaction $CsPbI_3$ crystallizes in its thermodynamically stable, non-emissive δ-phase,[38] but it does not seem to negatively influence the end products, once the perovskite is encapsulated inside the boron nitride nanotubes. Prior to encapsulation, BNNTs were annealed for 30 minutes at 250 °C in an open ceramic crucible under an Ar atmosphere to remove volatile contaminants. A large excess of perovskite and precleaned BNNTs were placed into separate parts of a quartz tube inside the glovebox. The quartz tubes were sealed under vacuum and the samples were annealed at approx. 50 °C above the melting point of the perovskite for at least 12 hours. The perovskite-filled nanotubes were kept in an inert atmosphere and processed freshly into films in air right before the PL measurements, unless otherwise stated in the respective sections.

Scanning transmission electron microscopy

Scanning transmission electron microscopic (STEM) measurements were carried out in an aberration-corrected 200 keV THEMIS microscope capturing energy dispersive X-ray spectra (EDS), high-angle annular dark field (HAADF) and spectrum images of the filled BNNTs. The perovskite@BNNTs for the STEM measurements were sonicated in toluene for separation, and then a drop of this toluene dispersion was placed on the surface of distilled water. A lacey carbon covered Cu-TEM grid was then pulled through perpendicularly to this surface toluene layer containing the dispersed BNNTs, resulting in an

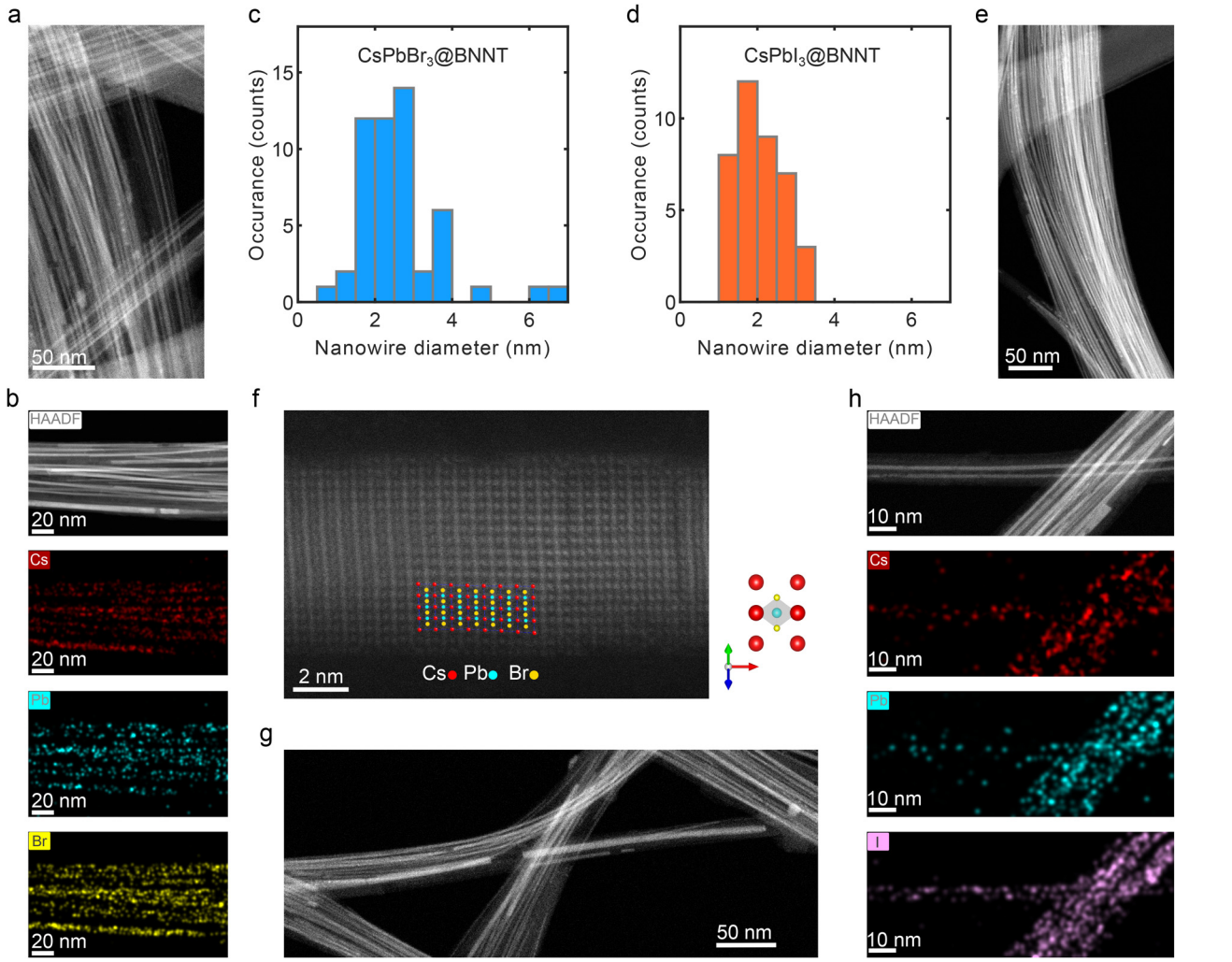

Fig. 1 High-angle annular dark field scanning transmission electron microscopy images and elemental maps of (a and b) $CsPbBr_3$@BNNT and (e and h) $CsPbI_3$@BNNT. (c and d) Samples presented are not DMF-washed, elemental analysis was performed on areas free from external particles. Distribution of the observed perovskite nanowire diameters based on a larger number of HAADF STEM images. (f) HAADF image of $CsPbBr_3$@BNNT and fitted model based on ICSD-201285 entry from the Inorganic Crystal Structure Database. The lattice is cubic, with a lattice parameter of 5.87 Å, the nanowire is 8–9 unit cells thick, and the nanowire is aligned with the [1 0 0] direction parallel to the nanotube axis. The unit cell in the corresponding orientation is displayed on the right. (g) Larger overview showing the same nanowire as on (f). Data on mixed halide samples are presented in Fig. S1.

ideal TEM sample of separated nanotubes and small bundles (later referred to as Langmuir–Blodgett-like coating). Finally, for images displayed in Fig. 1, the TEM grids containing the samples were annealed at 180 °C in dynamic vacuum for 4 days prior to the STEM measurements to eliminate any potential organic contamination. Imaging was performed both on freshly prepared samples and repeated after about one month of air storage, and no sign of degradation was observed.

Photoluminescence spectroscopy

To exclude environmental effects, photoluminescence spectra in an inert atmosphere were recorded of all as-synthesized samples before further use. For measurements inside an Ar-filled glovebox, a BWtek Exemplar spectrometer connected to a home-built optical setup was used. 405 nm excitation was provided by a 5 mW diode laser without focusing and the emission was filtered using a 450 nm longpass filter.

Hyperspectral maps for correlative micro-Raman/PL measurements on a small bundle were obtained using a Bruker RAMANtouch microscope. 532 nm excitation with 4 mW power was used with a 100× objective. 15–20 spectra were averaged for each area along the nanotube, which were chosen based on overlaying the hyperspectral map with the atomic force microscopy (AFM) topography image. The full hyperspectral dataset was 37 × 53 pixel recorded with 0.2 µm step size and 3 s integration time for each spectrum. Quasar software was used for basic linear baseline correction, data visualization, and area averaging.[39]

Temperature-dependent photoluminescence spectra were obtained using a Horiba Nanolog fluorometer equipped with a nitrogen-cooled cryostat. Perovskite@BNNT samples for these measurements were sonicated in toluene until dispersed and spin-coated onto precleaned silicon slides. The substrates were cleaned by sonication in acetone and methanol for 5–5 minutes and dried with nitrogen prior to spin coating. Clean perovskite@BNNT samples were prepared by soaking the coated Si slides in a high excess of *N*,*N*-dimethyl formamide (DMF), exchanging the solvent several times, completed by a final rinse in toluene.

Photoluminescence imaging

PL imaging was performed using a modified Nikon Eclipse E600 POL microscope. Excitation was provided by a 385 nm LED (New Energy, LST1-01G01-UV02-00) in combination with a 380 nm center wavelength 10 nm bandpass optical filter. On the emission side either various longpass filters (400 to 700 nm, every 50 nm) or a bandpass filter (460 nm center wavelength, 60 nm bandwidth) was used. Monochromatic images were recorded using a QYHCCD QHY294 M-Pro camera and color images were obtained using a Canon Powershot G10 connected to the microscope. Samples were deposited on a Si wafer using the Langmuir–Blodgett-like coating technique described in the STEM section. Image series for the polar plots were collected using a 400 nm (Br) and a 550 nm (I) longpass filter on the emission side. Image processing consisted of the following steps: dark subtraction, realignment of the images to account for sample drift, noise reduction using 2D median filtering and background subtraction. A constant value was subtracted as background from each image, based on the average intensity of background pixels calculated in a larger area near the bundle with no sample on it. The subtracted background offset showed no polarization. Polar plots show pixel intensities summed in the region of the indicated bundle section.

Raman spectroscopy

Raman measurements were carried out on a Renishaw 1000 and a Renishaw InVia micro-Raman spectrometer using 488, 532, 633 and 785 nm lasers and a 50× objective having 0.5 and 0.55 numerical apertures. The laser power was kept low enough to prevent heating-induced shift of the Raman peaks and sample damage. Typical powers used for nanowire@SWCNTs and reference SWNCTs were 0.45 mW for 488 nm and 532 nm, 0.09 mW for 633 nm and 0.9 mW for 785 nm excitation. Bulk perovskites were measured using a 785 nm sub-bandgap excitation and laser powers below 0.3 mW.

Infrared spectroscopy

Infrared spectra were obtained using a Bruker Tensor 37 Fourier-transform interferometer connected to a Bruker infrared microscope using a HgCdTe detector with 4 cm^{-1} spectral resolution. The spectrum was recorded on the $CsPbBr_3$@BNNT sample used for PL imaging.

Atomic force microscopy

AFM topographic images were recorded using a Neaspec neaSNOM and a neaSCOPE instrument. The scan size was set to 25 × 25 μm with 1000 × 1000 pixel resolution. For the correlative AFM-micro-Raman/PL measurement, the AFM map was recorded with 23 nm pixel size. The height profile of the topographic image is commonly used to identify individual nanotubes in SWCNT samples, although it has some limitations in BNNTs. Due to their multi-walled structure and wider diameter range, the diameter of the inner cavity cannot be exactly determined. Up to 8 nm outer diameter we assigned structures as single nanotubes. Above this, large diameter single tubes and few nanotube bundles containing smaller diameter nanotubes are hard to distinguish.

Results and discussion

Synthesis of well-defined perovskite quantum wires inside BNNTs

Perovskite quantum wires were grown from the vapor phase inside narrow-diameter highly purified boron nitride nanotubes. We chose this method rather than the previously reported solution-based filling,[29] as the vapor-phase method results in higher filling ratios and long, continuous wires that are more suitable for applications and optical studies. We have developed the synthesis protocol for the production of these nanowires in BNNTs based on the high-temperature filling used earlier for carbon nanotubes.[28] Fig. 1 and Fig. S1 show STEM HAADF images demonstrating that the method is suitable for synthesis of high aspect ratio quantum wires in single and also mixed halide configurations inside BNNTs. As typical of template-confined synthesis methods, the nanowire size is critically controlled by the host nanotubes' diameter. In our case, quantum wires with a diameter of 1 to 9 unit cells are detected in the high-angle annular dark-field scanning transmission electron microscopy images (Fig. 1c and d), with the 2 × 2 and 3 × 3 unit cell thicknesses being the most abundant species, indeed corresponding to the typical inner diameters of our BNNTs of 1.5 to 8 nm. Interestingly, the nanowire diameters cover the range achievable in the smallest pore size alumina matrices and the single unit cell thick perovskites, previously synthesized in SWCNT hosts.[6,28,29] To unravel the structure of the encapsulated nanowires, atom-resolved HAADF images were recorded. Fig. 1f shows a $CsPbBr_3$ quantum wire section in a larger BNNT host. The quantum wire is α-phase, with its [1 0 0] axis parallel to the nanotube. The STEM images show efficient filling, further supported by the additional energy dispersive X-ray spectroscopy (EDS) analysis (Tables S1–S3). The apparent length of most quantum wires is on the order of hundreds of nanometers, meaning most wires have an aspect ratio that well exceeds 100. This is a lower estimate, as the exact wire lengths cannot be precisely determined based on the STEM images due to their very high aspect ratio and bundled

appearance. The host BNNTs have a length of up to a few microns, which defines an upper limit for the achievable aspect ratio on the order of thousands.

Optical properties of the encapsulated quantum wires

By using BNNT hosts, as opposed to carbon nanotubes, the optical transparency and large bandgap inherently do not affect the optical properties of the nanowires, making it possible to detect direct emission from inside the BNNTs.

As demonstrated by the photos in Fig. 2a obtained from the $CsPbBr_3$ and $CsPbI_3$-filled BNNT samples after encapsulation, the emission of the perovskite wires is significantly blue-shifted compared to their bulk counterparts, due to the strong quantum confinement. BNNT-confined $CsPbBr_3$ emits in deep blue and $CsPbI_3$ in an orange color, while their bulk counterparts have a green and deep red fluorescence. The corresponding PL spectra recorded inside the glovebox, before the samples were exposed to any solvents or ambient atmosphere, are shown in Fig. S3. The blue-shifted emission of the quantum wires is in line with the expectations, because based on the size distributions in Fig. 1c and d, the wire diameters are well below the Bohr radius of the excitons, which is approximately 7 and 12 nm for $CsPbBr_3$ and $CsPbI_3$, respectively.[11] However, the vapor-phase synthesis yields encapsulated quantum wires and also a large number of nanoparticles of various sizes adsorbed onto the nanotube bundles (Fig. S2a), which are later clearly removed in the post-processing. Nevertheless, the emission of the confined wires dominates even the unwashed samples.

Dominance of the quantum wire emission might be expected in the case of $CsPbI_3$, where the solid-state synthesis resulted predominantly in the formation of the non-emissive δ-phase on the outside surface of the nanotubes, even the precursor perovskite used for the filling was in this phase (Fig. S4). However, inside the nanotubes the confinement can facilitate the formation of thermodynamically unstable structures,[28,29] and the encapsulated $CsPbI_3$@BNNT quantum wires show orange emission upon UV illumination. Additionally we observed significantly fewer adsorbed nanoparticles in the STEM images in this case than in the bromide-based samples.

$CsPbBr_3$ is somewhat different, as it crystallizes in an emissive phase both outside and inside the nanotubes. Nevertheless, the expected green photoluminescence of the non-encapsulated particles is almost undetectable on the as-prepared samples, despite an abundance of $CsPbBr_3$ nanocrystals of various sizes being present (Fig. S2a). Based on the size distribution of the non-encapsulated species (Fig. S2c), their PL is expected to arise predominantly above 500 nm, with minor contribution in the blue region from sub-6 nm particles.[40,41] The lack of luminescence originating from adsorbed nanoparticles in the spectra of the as-prepared $CsPbBr_3$@BNNT samples potentially stems from their high surface to volume ratio and unprotected, highly defective

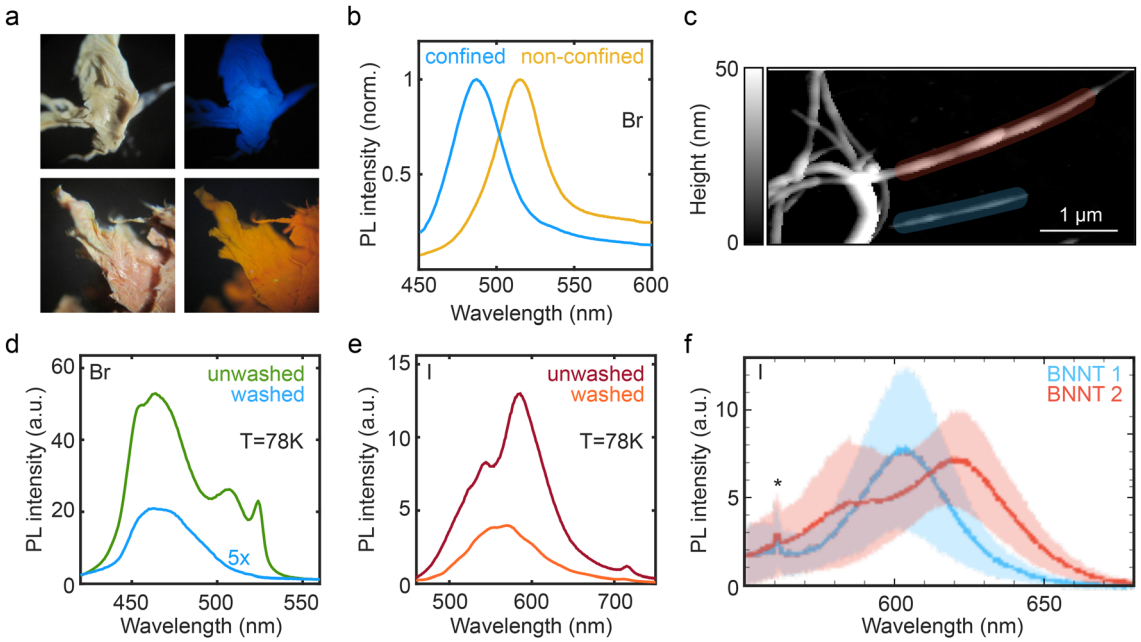

Fig. 2 Photoluminescence of the encapsulated quantum wires. (a) Photos under white light and 380 nm UV illumination of the $CsPbBr_3$@BNNT (top) and $CsPbI_3$@BNNT samples (bottom) after encapsulation. (b) Photoluminescence of confined and non-confined $CsPbBr_3$ samples normalized to the intensity maximum. The former are encapsulated in BNNTs, the latter sample dominantly contains emitters that are entangled in a hBN network surrounding the BNNTs. (c) AFM topography recorded on the $CsPbI_3$@BNNT sample deposited onto Si. Photoluminescence spectra comparing emission from unwashed and DMF-washed perovskite@BNNT quantum wires at 78 K, (d) $CsPbBr_3$@BNNT and (e) $CsPbI_3$@BNNT. (f) Averaged micro-PL spectra and their distribution recorded in a single BNNT (blue area) and a small bundle (red area) marked in (c). The peaks indicated by * correspond to the Raman scattering of the Si substrate.

surface. We note that these particles have no passivating layer, contrary to the highly emissive perovskite nanoparticles commonly shown in the literature, which becomes even more apparent, when the samples are processed, as discussed in later sections. In contrast to the defective nanoparticles on the outer surface of the nanotubes, the confined perovskite quantum wires are well-protected from the environment, therefore their emission dominates the spectra. To further support that the emission originates from the encapsulated quantum wires we compare the emission of $CsPbBr_3$ prepared under identical conditions but in different BNNT hosts. While both BNNT samples have a similar diameter distribution, one contains much shorter nanotubes and a significant amount of hexagonal boron nitride (hBN) sheets as a result of the opening procedure, resulting in blocked tube ends preventing efficient filling. The corresponding STEM and TEM images in Fig. S5 display that a large amount of perovskite nanoparticles is entangled in this network of hBN, which creates a similar protective layer around them as the nanotubes, but without the strong confinement effect. Accordingly, this reference sample is luminescent, but the emission is centered closer to the bulk value, at 514 nm, as shown in Fig. 2b.

For further optical measurements we applied thorough washing of the samples in DMF, which is a good solvent for perovskites, to remove the adsorbed species. Fig. 2f shows micro-PL spectra recorded on single perovskite-filled nanotubes and small bundles, which were identified using atomic force microscopy based on their height profile, as described in the Experimental section. We estimated the number of quantum wires present in typical bundle sizes based on the STEM images. Structures up to 12 nm outer diameter contain typically 1 to 2 quantum wires, and under 20 nm outer diameter we expect 1–4 quantum wires to be present. The blue-marked area in Fig. 2c is identified as a single BNNT with 8 nm outer diameter; the red-marked bundle has an overall diameter of 20–30 nm on most parts. The emission spectra recorded on the individual BNNT and the small bundle are displayed in Fig. 2f. Emissions identified are centered around 585, 600 and 620 nm. As a comparison, 2.2 nm and 4 nm wide free-standing nanorods in solution were reported to emit at 580 and 626 nm, respectively.[5,13] These would reasonably fit inside the displayed hosts and are in line with the observed diameter range based on the STEM data.

The width of the emission peak on the single tube is approximately 100 meV. Size dependent PL broadening of small perovskite nanoparticles was described before and attributed to increased coupling to localized phonon modes arising from undercoordinated surface atoms.[42] To the best of our knowledge, there are no PL spectra of single perovskite quantum wires having a comparably small diameter available in the literature. As a comparison, the emission linewidth on an ensemble of highly uniform 2.2 nm diameter $CsPbI_3$ quantum wires was around 150 meV in ref. 13. To exactly match the quantum wire diameter and surface structure with the emission properties future detailed studies are needed, for example using cathodoluminescence recorded in a STEM setup, where the wire diameter can be visualized and directly linked to the emission. The BNNT-encapsulated perovskites would be ideal candidates for such experiments due to their enhanced stability compared to free-standing nanowires.

Additional PL measurements on ensembles of perovskite@BNNTs were also performed to provide information about the distribution of the quantum wire emission and its temperature dependence. In ensembles it is often complicated to assess if the detected emission originates from inside the nanotube or from the non-encapsulated species.[43,44] We applied a thorough washing to largely remove the adsorbed species and present data both on washed and unwashed samples to identify the signals arising from the encapsulated species and discard those from the limited amount of the non-encapsulated material. Choosing appropriate solvents is of utmost importance to avoid alterations of the perovskite structure, which can significantly influence the observed photoluminescence. We include a short discussion about the washing procedure, the potential byproducts and their emission in the SI (a note on the formation of byproducts).

Fig. 2d and e display PL spectra of perovskite@BNNT samples spin-coated onto silicon wafers from toluene before and after DMF washing, respectively. The complete temperature-dependent measurement series between 78 and 300 K are shown in Fig. S7a–d. At room temperature, the emission of the quantum wires is preserved after washing. Some intensity decrease is expected, because some of the carrier nanotubes can get removed from the surface during washing. However, at low temperatures, the presence of non-encapsulated species and their contribution becomes apparent. By comparing the spectra of washed and unwashed $CsPbBr_3$@BNNT in Fig. 2d and e and in Fig. S7a and c, two green emission peaks (at 2.41 and 2.38 eV, 513 and 522 nm, at 78 K) can be clearly distinguished below 260 K, which are not detected after washing of the samples and therefore can be assigned to originate from non-confined outer particles. Extended exposure to DMF can cause some damage to the encapsulated quantum wires as well, especially those in larger diameter host nanotubes. Therefore, besides removal of the adsorbed species, this can also contribute to the small overall blue shift of the observed PL distribution. This effect is especially pronounced in the case of $CsPbI_3$@BNNT. Emission of PbI_2 byproducts that can form as a result of degradation of the non-encapsulated perovskites gives a contribution in the high energy region of the spectra, where the shoulder around 506 nm (2.45 eV) significantly decreases after washing. In summary, the main emission features of the BNNT-confined $CsPbBr_3$ nanowires are located between approximately 440 and 490 nm, with some contribution around 500 nm originating from larger nanowires, overlapping with the emission external particles. $CsPbI_3$@BNNT shows emission from approximately 530 to 640 nm. External particles emit dominantly around 700 nm and above, but degradation byproducts can overlap with the emission of the smallest nanowires.

The strong temperature dependence of the PL intensity of the non-confined nanoparticles potentially stems from the

defective nature of their surface. The thermal PL quenching at room temperature makes the emission of the non-encapsulated $CsPbBr_3$ nanoparticles undetectable, when a high enough excitation energy is used that can be absorbed by the encapsulated quantum wires as well. The green emission of the non-encapsulated species shifts towards higher energies with increasing temperature, in line with earlier results obtained on larger $CsPbBr_3$ nanoparticles.[45] This shift arises from the increase of the bandgap due to thermal dilation of the lattice and the contribution of exciton-phonon coupling. The emission of the quantum wires, on the other hand, shows a significantly smaller shift with temperature and in the opposite direction. Similar temperature dependence has been reported in strongly quantum-confined perovskite particles[41] and interpreted as the result of the opposing contribution of acoustic and optical phonons to the temperature dependent bandgap. To further demonstrate this behavior, temperature-dependent PL spectra of a core–shell $CsPbBr_3$@$CsPb_2Br_5$ system containing both strongly and weakly quantum-confined emitters are shown in Fig. S7e as a reference. The atypical shift of the PL of the BNNT-encapsulated quantum wires therefore potentially primarily stems from their narrow diameter. Interaction with the host BNNTs, such as the mechanical constraints or the altered exciton–phonon coupling, potentially plays a role in the temperature evolution of the emission. To unravel these host-specific effects, samples prepared in BNNTs with a narrower inner diameter distribution would be needed. $CsPbI_3$ quantum wires show similar behavior to the bromide ones: shifts observed in the emission of the quantum wires by changing temperature are in a direction opposite to those in larger nanoparticles. Fig. S8 shows the normalized photoluminescence of the bromide and iodide-based quantum wires between 78 and 300 K. Overall, BNNT-encapsulated quantum wires demonstrate good chromatic stability in a wide temperature range, which is advantageous for optical applications.

Compared to free-standing perovskite quantum wires of similar diameters,[5,13–15,46] both perovskite@BNNT ensembles show a slightly red-shifted PL at room temperature, although the literature values scatter significantly. Typically, the emission energies measured on the BNNT-encapsulated perovskites are more in line with quantum wires having a cross-section of 3 to 5 unit cells (2.3–4 nm). The diameter distribution measured on the STEM images is shown in Fig. 1. Several factors can contribute to this slight red shift of the emission wavelength. The primary is the dielectric environment around the perovskite quantum wire, which influences the exciton binding energy and therefore the energy of the PL. Additionally, since the perovskites are only a few unit cells wide, the surface states strongly influence the photoluminescence quantum yield of the wires, and a significantly higher apparent contribution of larger wire diameters in the PL spectra is expected in the case of mixed diameter ensembles.[15] Furthermore, the aspect ratio of the nanowires can have an influence: increasing the length of the wires of the same diameter was shown to result in a red shift of their emission.[27]

Comparison of boron nitride and carbon nanotube hosts

Carbon and boron nitride nanotubes are structural analogues, but their electronic structure is very different; therefore comparison of these two hosts can provide further insight into the origin of the PL. The BNNTs used here are multi-walled, unlike the carbon nanotubes, but in the scope of the comparison only their inner diameter matters. The diameters present in our BNNT sample include the 1.2–2 nm range of the SWCNTs used for perovskite encapsulation and larger tubes up to 8 nm. BNNT nanotubes form a core–shell system with the perovskites, where the perovskite is surrounded by a higher bandgap material, which is significantly different from SWCNT-encapsulated perovskite wires. SWCNTs, having a significantly lower bandgap than the perovskite quantum wires, are expected to provide an easy channel for charge and energy transfer, especially when non-sorted SWCNTs are used, in which on average one third of the nanotubes are metallic. Charge transfer between the photoexcited perovskites and carbon nanotubes was observed both on CNT-perovskite composites and perovskite@CNT systems.[7,47,48] Two recent publications showed weak emission from perovskite@SWCNT heterostructures.[48,49] It was proposed that the origin of the luminescence is either a surface trapped exciton state or an interlayer exciton formed due to the type II band alignment of the SWCNT and the perovskite, thus making the system emissive.[49] Regarding the latter explanation, we note that the structure of the quantum wire surface, especially the Cs vacancies and the chirality of the host nanotube, can significantly alter the band alignment between individual perovskite quantum wire and host nanotube pairs, especially in $CsPbI_3$@SWCNT.

Besides perovskite-filled BNNTs, we also prepared $CsPbBr_3$@SWCNT with similarly good filling yield (Fig. S9a, b and Table S5). Description of the sample preparation and more details on the characterization are included in the SI's respective section ($CsPbBr_3$@SWCNT). Evidence of significant charge transfer between the perovskites and the host carbon nanotubes was detected in the shift of the G and 2D bands on the Raman spectra (Fig. S9d) similar to earlier reports.[7,30,48] Fig. S9c displays the emission spectra of the unwashed $CsPbBr_3$@SWCNT sample. We did not observe photoluminescence at room temperature, but upon cooling to low temperature, an emission peak at 524 nm, close to the position reported in ref. 48 appeared. Its temperature dependence and position were the same as the non-encapsulated particles in the BNNT sample. The significant difference compared to $CsPbBr_3$ in the BNNT host is the lack of blue emission from the carbon nanotube-based samples, although the encapsulated wires have diameters in the strongly quantum-confined range inside the sub 2 nm diameter SWCNT hosts. Interlayer excitons can account for the lack of significant blue shift in the emission, because in this case the confinement effects can be lost, but comparison of the washed and unwashed samples demonstrates that the observed green emission is not detectable after thorough washing (Fig. S9e). In conclusion, our findings do not support that the observed green photo-

luminescence would originate from the SWCNT-encapsulated $CsPbBr_3$ perovskite quantum wires.

In ref. 49 a series of PL peaks was reported to originate from single-walled carbon nanotube-encapsulated single unit cell wide $CsPbI_3$-based perovskite quantum wires. Due to the smaller bandgap of the iodide-based perovskite, the heterojunction formed with the carbon nanotube can be different from that in the bromide case. The position of peak E_1 in Fig. 4 of ref. 49 overlaps in energy partially with the DMF-washed $CsPbI_3$@BNNT at 77 K (around 2.2 eV, 563 nm) and shows similar temperature dependence. Inside BNNT hosts however, the temperature dependence of the PL intensity is much less pronounced compared to SWCNTs. Overlap in energy is expected, as the smallest quantum wire sizes present inside BNNTs can be accommodated by SWCNTs as well, and their contribution is enriched after intense washing. The spectra of $CsPbI_3$@BNNT contain the contribution of several other encapsulated emitters as well due to the BNNTs' wider diameter range, for example from larger quantum wires on the lower energy side, around 2.07 eV (598 nm). Because of the inherently broad emission of the quantum wires the different contributions are hard to separate. Especially peaks in the high energy part of the spectra, also shown in ref. 49, need careful assessment, as PbI_2, a potential degradation product, has emission in this range. The slight shoulder around 2.45 eV (507 nm) at low temperature can occur due to the presence of PbI_2 (Fig. S5c), and the contribution from this region decreases significantly upon DMF washing in our BNNT hosted samples (Fig. 2d). Future single tube studies with an appropriate excitation wavelength are needed to decisively conclude the origin of these higher energy emission peaks and to identify if the emission of the smallest single or half unit cell wide quantum wires can be detected or not.

Overall, boron nitride nanotubes are more suitable nanocontainers than their carbon counterparts to create emissive heterostructures, demonstrating a strong luminescence even at room temperature. Due to the strong steric confinement inside nanotubes the quantum wires can possess a variety of termination structures along the confined dimensions, which are not achievable on free-standing nanowires.[28] This can significantly alter the band alignment between the host and the guest in a composite system and therefore change the emission properties. BNNTs can provide a unique platform to study the optical properties of these defect sites on individual quantum wires.

Polarization anisotropy of the encapsulated quantum wires

An important technologically relevant property of perovskite nanowires is their optical anisotropy.[9,50] Individual quantum wires or small bundles can be used as nanoscale polarized light sources. Fig. 3a displays polarized PL images of $CsPbBr_3$@BNNT bundles deposited on silicon. Infrared

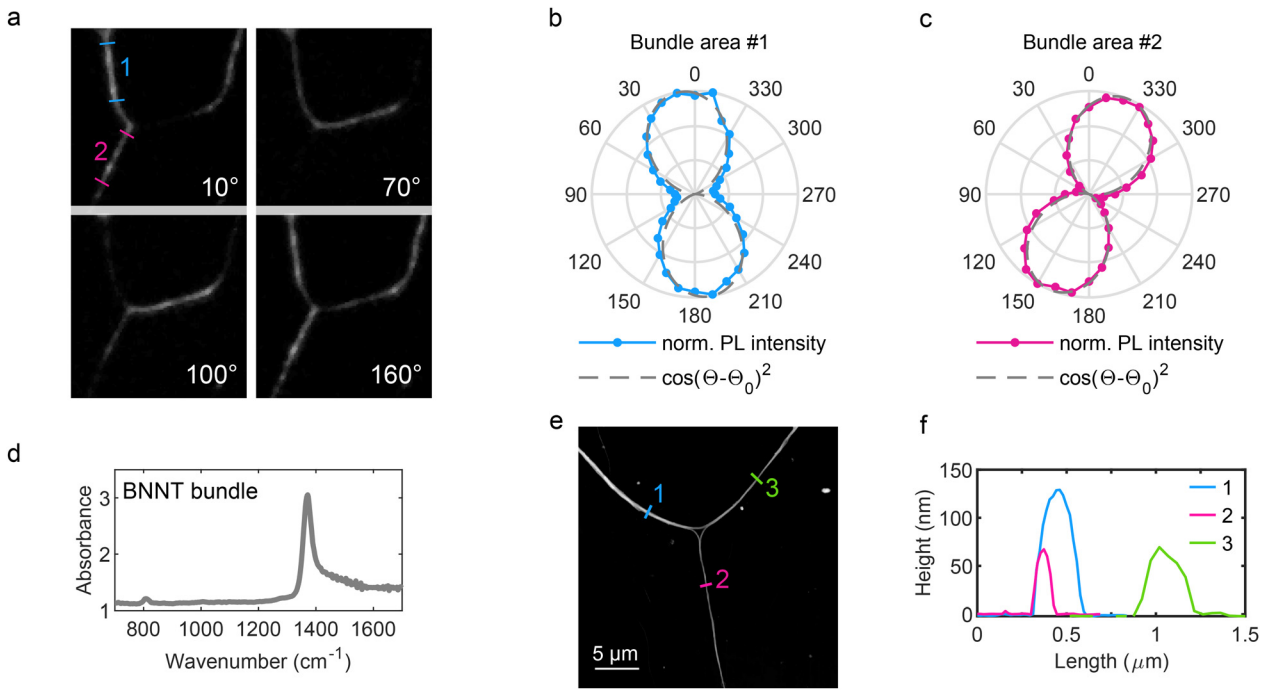

Fig. 3 (a) Polarized photoluminescence images of a $CsPbBr_3$@BNNT bundle. Analyzer settings are displayed on the images. Excitation was provided by a 380 nm LED and emission was filtered using a bandpass filter having 460 nm center wavelength and 60 nm bandwidth. (b and c) Polar plots of the photoluminescence of two, almost linear bundle sections, 1 and 2 as marked in a. The scale is normalized to the intensity maximum. The corresponding image series and additional polar plots are shown in Fig. S10, S11 and S12. Images were recorded at room temperature in air. (d) Infrared absorption spectrum recorded on characteristic luminescent filaments showing modes of boron nitride nanotubes. (e) AFM topography of the same bundle region and (f) line profiles extracted from it.

spectra recorded on a set of characteristic filaments (Fig. 3d) show the out-of-plane radial buckling mode at 803 cm^{-1} and the in-plane stretching mode at 1375 cm^{-1} characteristic of BNNTs.[51] Based on atomic force microscopy topography (Fig. 3e and f) the imaged structures are on the order of a hundred nanotubes. The imaged areas for the polar plots (Fig. 3b and c) were chosen to represent predominantly straight sections of the bundles. These bundles of quantum wires are showing a highly linearly polarized emission, independent of the bundle size, which suggests the individual nanowires to be polarized emitters, as expected. The major contribution to the anisotropy is presumably the high aspect ratio of the individual confined nanowires that can be improved by the natural alignment of the BNNTs into bundles. The anisotropy of the emission is not affected by being exposed to ambient conditions. Some samples were exposed to air for days during repetitive measurement sessions and showed no PL intensity loss. Similar results were obtained on $CsPbI_3$ quantum wires (Fig. S12). As a reference we also recorded a polarization series on one of the observed isolated green emitters on a $CsPbBr_3$@BNNT sample, which showed no polarization dependence at room temperature (Fig. S11).

Stability and processability

Boron nitride nanotubes can support the formation of well-defined quantum wires and also stabilize their structure. Degradation of perovskite quantum wires primarily occurs for the following reasons: exposure to humidity and processing chemicals, coalescence, ripening and morphological changes, and heat induced damage.[16,52–55] Exposure to humidity can result in conversion into non-emissive $CsPb_2Br_5$ and CsBr. Initially, water molecules passivate the surface defects, thus resulting in a transient state with increased photoluminescence quantum yield, which can be used to visualize the non-encapsulated perovskites on the surface-coated films. If only a limited amount of water is available, high quantum yield core–shell nanoparticles can form as intermediate steps, where $CsPbBr_3$ nanoparticles are embedded in larger $CsPb_2Br_5$ shells.[52] We used water-treated perovskite particles for the temperature dependent PL experiments as a reference material, as they are quite stable against further environmental degradation. As a reference to compare the stability of the encapsulated quantum wires, we also prepared oleic acid coated nanoparticles of similar sizes using the method presented in ref. 56 and processed them similarly to the BNNT-encapsulated quantum wires. $CsPbI_3$ nanoparticles were unstable and degraded in a few hours when kept in the original solution in air. The $CsPbBr_3$ nanoparticles were more stable in the toluene solution, but upon coating them onto silicon, the dry samples quickly lost most of their luminescence in air, in line with earlier stability studies on individual particles.[18,57] In contrast, perovskite@BNNT samples that were imaged by STEM after over a month of air storage still retained the perovskite structure (Fig. 1f), and their luminescence was preserved even after months of storage in air (Fig. 4b). We also observed improved stability on samples where perovskites were entangled in a network of boron nitride sheets (Fig. S5), but were mostly not encapsulated. The latter samples, however, do not withstand washing, as the protective network of hexagonal boron nitride sheets rapidly disintegrates. Perovskite@BNNT

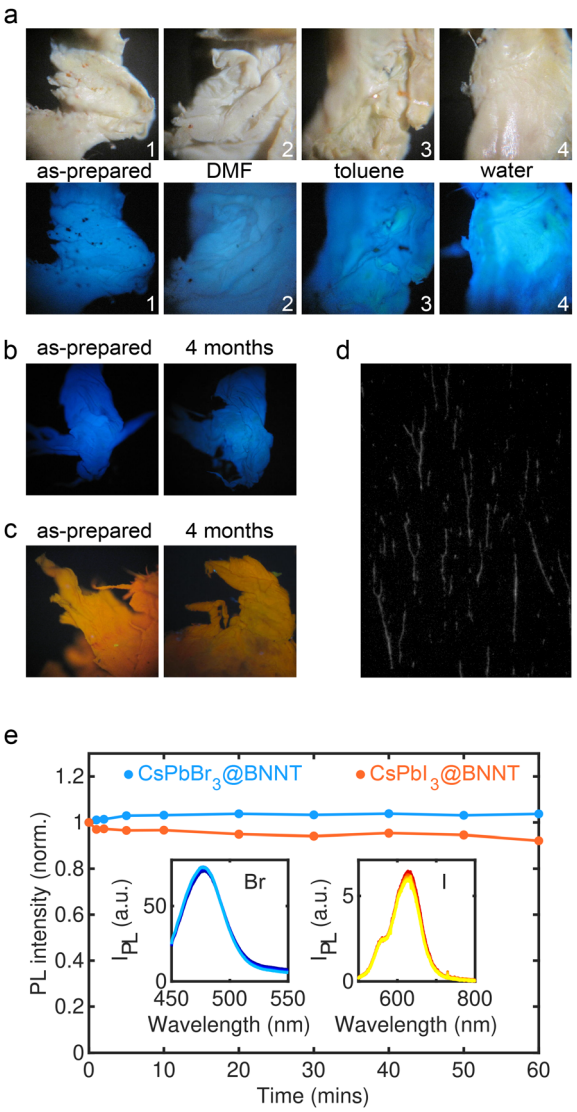

Fig. 4 (a) Bright light and photoluminescence images of $CsPbBr_3$@BNNT as-prepared and after soaking for 10 minutes in various solvents. The sample presented in (a) is from an earlier batch, having also larger perovskite crystals entangled in the BNNT network. These orange-colored embedded crystals appear as dark areas or green in the PL images. The green emission after solvent exposure is the result of solvent etching of their surface. PL images of (b) $CsPbBr_3$@BNNT and (c) $CsPbI_3$@BNNT samples as-prepared (left) and after 4 months storage in air (right) demonstrate very good stability. (d) PL image of aligned $CsPbBr_3$@BNNT bundles deposited from the water–toluene interface. Excitation was provided by a 380 nm LED and emission was filtered by a bandpass filter with the transmission range of 430 to 490 nm. (e) Photoluminescence intensity measured upon 1 hour continuous illumination inside a glovebox on unwashed $CsPbX_3$@BNNT samples using 405 nm laser excitation at 5 mW with a laser pointer. The graph is normalized to the intensity of the first measurement. Insets are showing the corresponding PL spectra.

samples also show stable emission performance, as shown in Fig. 4e. The experiments displayed were done on the as-prepared sample without exposure to solvents or ambient environment to rule out extrinsic effects. The stable emission of the nanowires is not specific to the BNNT encapsulation; similar stability can be observed from small perovskite nanoparticles embedded in a hBN network (Fig. S14). However, as indicated earlier the hBN network does not withstand further solvent processing. Small bundles imaged in air also show good stability. The image series displayed in Fig. S10 and S12 were typically recorded over an hour or two, while the sample was continuously illuminated.

The next important issue with stability of small diameter nanoparticles or nanowires is coalescence or ripening. This can be completely prevented by BNNT encapsulation. Morphological instabilities of the wires often cause problems, such as loss of the polarization anisotropy.[16,58] No such stability issues were found in our study over the measurement period of 4 months, because of the protection provided by the BNNT hosts.

The significant advantage of BNNT encapsulation compared to any molecular surface passivation is that even if the quantum wires would eventually deteriorate with time, they can be regenerated. As long as the CsBr byproduct of the reaction is kept confined in the system, water-degraded perovskite phases can be reversed by drying the sample. This property is well-established for perovskites encapsulated in stable porous bulk materials,[59] but with the nanotube encapsulation this can be achieved on a single quantum wire level, which is unique. Morphological changes are similarly repairable by reannealing. BNNTs are stable up to much higher temperatures both in a vacuum and in air than the melting point of the bulk perovskites.[60] Besides being stable up to 800 °C in air, they also have excellent thermal conductivity,[61,62] which can further increase the stability of the quantum wires under extended illumination.[37] In this respect, BNNTs can considerably outperform mesoporous silica, MOFs or porous alumina membrane hosts.[63,64]

BNNT encapsulation significantly improves the processability of the quantum wires. The walls of the BNNTs are impermeable for gases and solvents, but post-synthesis closing of their open ends is still a challenging problem. Nevertheless, due to the narrow inner diameter and the very high aspect ratio of the nanotubes, enough protection is provided for the inner quantum wires to allow further processing in appropriately chosen solvents. Boron nitride nanotubes themselves have exceptional chemical stability, therefore the choice of solvents is solely limited by the perovskite. As shown in Fig. 4a, the BNNT-encapsulated quantum wires can withstand extended soaking in water and toluene, but DMF soaking introduces some decrease in their luminescence.

BNNT-encapsulated nanowires can be dispersed using sonication. The multi-walled BNNTs are significantly less affected by sonication-induced damage than SWCNTs, where even a few minutes of bath sonication can induce nanotube breaking and opening.[65,66] Sonication in solvents that are inert for the perovskites, such as toluene, does not adversely affect the integrity of the quantum wires within the time frame necessary to separate the BNNTs. This is in contrast to molecular encapsulation, where guest molecule leaching from the BNNTs during post-processing is a common problem, due to the weaker interactions with the boron nitride host compared to carbon nanotubes.[34,51] We found that extended sonication in DMF can adversely affect the encapsulated quantum wires. Alternatively, if harsher solvents are to be used for example to create highly aligned BNNT patterns, the hosts can be first processed to the desired form, such as deposition onto surfaces in a specific pattern, *etc*. and the quantum wire synthesis can be performed afterwards. A similar approach was previously demonstrated on fluorescent dye-filled BNNTs.[32]

Adsorbed particles can be efficiently removed after BNNT deposition by a short soaking in DMF (Fig. 2). Water and alcohol should be avoided in the washing procedure, as they are primarily AX-selective solvents (A: MA/Cs, X: halogen), therefore can cause cesium loss,[55] are not efficient to remove the lead halide residues from the outside of the nanotubes, and can contribute to activating luminescence of non-encapsulated species, as we discussed earlier.[67] In contrast to free-standing wires, where the smallest diameter species are typically the most vulnerable during the washing steps,[15] smaller diameter BNNT hosts provide greater protection, therefore extensively washed samples can be enriched in narrower quantum wires. We observed a diameter decrease of the ensemble in iodide-based wires, which have generally somewhat lower stability than the bromide alternative. Thus, despite BNNTs are available in a wide range of inner diameters, the best protection can be achieved using narrower nanotubes.

Finally, we highlight some of the technologically relevant properties of our BNNT-encapsulated perovskite quantum wires. Due to the high level of protection provided on the individual quantum wire level, these structures are ideal building blocks for nanoscale photonic applications. Small bundles of BNNTs are ideal as light sources with increased luminescence, containing well-separated but highly aligned quantum wire emitters. Furthermore, large-scale highly flexible assemblies can be created by combining bundles of perovskite@BNNTs.[62] It was recently shown that BNNTs can be processed into aligned films and extruded into neat BNNT fibers after dissolution in chlorosulfonic acid,[68] or by spontaneous self-assembly following DNA-coating.[69] A milder treatment resulting in aligned BNNT bundles, that can be performed even after perovskite synthesis, is the alignment using the PMMA matrix[32] or by Langmuir–Blodgett-like coating from the water–toluene interface (Fig. 4d). While bulk matrices such as porous alumina or silica can have exceptional pore alignment and can demonstrate some flexibility,[25,70] a network of BNNTs are held together by weak van der Waals forces, therefore bending would mainly distort the network structure, not pores containing the quantum wires themselves. Lastly, BNNTs form an insulating tubular shell around the perovskite quantum wires, making them also ideal candidates for nanoelectronics.

Indeed, SWCNT@BNNT structures were prepared and suggested to be applied as miniature coaxial cables[51] and more sophisticated electronic components, *e.g.* transistors, were proposed based on MoS_2-SWCNT-BNNT heterostructures.[71] As the BNNTs are grown catalyst-free, the possible metallic content of the host would not interfere with such applications.

Conclusions

High aspect ratio perovskite quantum wires with well-defined structures and diameters in the strong confinement regime were synthesized in BNNTs, which allow access to the anisotropic emission of the perovskite wires. These individually encapsulated perovskite quantum wires serve as an ideal platform for advanced optical spectroscopy studies of structural alterations due to confinement. BNNTs form an excellent protective shell around perovskite quantum wires against environmental stressors, provide stability during necessary post-processing steps for device fabrication and facilitate regenerability all on a single quantum wire level. These heterostructures are ideal building blocks for nanoscale devices, as the nanotube shell isolates the quantum wires and prohibits inter-wire interactions. Perovskite@BNNTs are interesting candidates for novel photonic applications and for advanced optical studies on single quantum wire emitters. Individually encapsulated quantum wires or small bundles that naturally align the emitters can be used as nanoscale polarized light sources.

Author contributions

B. B. conceived the study and developed the methodology, prepared samples, conducted PL and Raman spectroscopy experiments, analyzed the data and created visualizations. E. D. designed and conducted transmission electron microscopy experiments, analyzed the data and created visualizations. G. N. conceptualized and conducted the single nanotube experiments and analyzed the data. M. S. prepared samples, conducted AFM, Raman and PL spectroscopy and PL imaging experiments, participated in the data processing and created visualizations. I. H. prepared samples and conducted PL experiments, assisted in data analysis and created visualizations. J. M. assisted in the conceptualization of the trial experiments, prepared samples and assisted with PL spectroscopy and imaging experiments. É. K. assisted in conceptualization of the project and prepared samples. F. B. supervised the single nanotube experiments and participated in the data processing. K. K. conducted the infrared experiments. All authors contributed to writing the manuscript, with B. B. preparing the initial draft and E. D., G. N., M. S., I. H., É. K., F. B. and K. K. providing critical revisions. B. B, E. D., É. K., F. B., and K. K. secured funding.

Conflicts of interest

There are no conflicts to declare.

Data availability

Data for this article, including TEM and AFM images, Raman, IR, PL spectra and photo series are available at https://repo.researchdata.hu/ at https://doi.org/10.5158/ARP/2CI6QD.

After the review process the data will be released for open access.

Supplementary information (SI): additional characterization details of STEM and EDS, Raman and PL spectroscopy, PL microscopy image series of the $CsPbX_3$@BNNTs and characterization of the $CsPbBr_3$@SWCNT sample. See DOI: https://doi.org/10.1039/d5nr05217c.

Acknowledgements

The authors thank partners at BNNT LLC for providing the high quality BNNTs.

The authors thank Áron Pekker and Mehmet Derya Özeren, who participated in conceptualizing the idea; Rohit Babar, Gábor Bortel, Sofie Cambré, Ádám Gali, Roland Fikó, Zsolt Fogarassy, Sándor Kollarics, Korbinian Kaltenecker and László Péter for additional characterization and discussions.

This research was supported by the National Research, Development and Innovation Office of Hungary-NKFIH, project no. OTKA K 143153, MEC_R_24 149054 and TKP-2021-NVA-04, financed under the TKP2021 funding scheme. Transmission electron microscopy was supported by the VEKOP-2.3.3-15-2016-00002 and VEKOP-2.3.2-16-2016-00011 projects.

References

1 J. H. Noh, S. H. Im, J. H. Heo, T. N. Mandal and S. I. Seok, *Nano Lett.*, 2013, **13**, 1764–1769.
2 H. Zhu, Y. Fu, F. Meng, X. Wu, Z. Gong, Q. Ding, M. V. Gustafsson, M. T. Trinh, S. Jin and X.-Y. Zhu, *Nat. Mater.*, 2015, **14**, 636–642.
3 Y. Fu, H. Zhu, C. C. Stoumpos, Q. Ding, J. Wang, M. G. Kanatzidis, X. Zhu and S. Jin, *ACS Nano*, 2016, **10**, 7963–7972.
4 A. I. Hochbaum and P. Yang, *Chem. Rev.*, 2010, **110**, 527–546.
5 A. Pramanik, S. Kundu, O. P. Kolawole, K. Gates and P. C. Ray, *Chem. Phys. Lett.*, 2024, **835**, 140952.
6 Q. Zhang, D. Zhang, Z. Liao, Y. B. Cao, M. Kumar, S. Poddar, J. Han, Y. Hu, H. Lv, X. Mo, A. K. Srivastava and Z. Fan, *Adv. Mater.*, 2025, **37**, 2405418.
7 K. Wang, Y. Zhao, L. Geng, H. Wang, Y. Teng, J. Yao, C. Zhou, X. Li, P. Zhao, Y. Wang, H. Liang, Y. Zhang, D. Tian and L. Kang, *ACS Nano*, 2025, **19**, 16110–16118.

8 C.-H. Lin, C.-Y. Kang, T.-Z. Wu, C.-L. Tsai, C.-W. Sher, X. Guan, P.-T. Lee, T. Wu, C.-H. Ho, H.-C. Kuo and J.-H. He, *Adv. Funct. Mater.*, 2020, **30**, 1909275.
9 X. Lu, J. Li, Y. Zhang, L. Zhang, H. Chen, Y. Zou and H. Zeng, *ACS Appl. Mater. Interfaces*, 2024, **16**, 24976–24986.
10 E. Horváth, M. Spina, Z. Szekrényes, K. Kamarás, R. Gaal, D. Gachet and L. Forró, *Nano Lett.*, 2014, **14**, 6761–6766.
11 L. Protesescu, S. Yakunin, M. I. Bodnarchuk, F. Krieg, R. Caputo, C. H. Hendon, R. X. Yang, A. Walsh and M. V. Kovalenko, *Nano Lett.*, 2015, **15**, 3692–3696.
12 D. Zhang, S. W. Eaton, Y. Yu, L. Dou and P. Yang, *J. Am. Chem. Soc.*, 2015, **137**, 9230–9233.
13 D. Zhang, Y. Yu, Y. Bekenstein, A. B. Wong, A. P. Alivisatos and P. Yang, *J. Am. Chem. Soc.*, 2016, **138**, 13155–13158.
14 M. Imran, F. Di Stasio, Z. Dang, C. Canale, A. H. Khan, J. Shamsi, R. Brescia, M. Prato and L. Manna, *Chem. Mater.*, 2016, **28**, 6450–6454.
15 H. Huang, M. Liu, J. Li, L. Luo, J. Zhao, Z. Luo, X. Wang, Z. Ye, H. He and J. Zeng, *Nanoscale*, 2017, **9**, 104–108.
16 M. Ng, S. B. Shivarudraiah and J. E. Halpert, *J. Mater. Chem. C*, 2022, **10**, 8947–8954.
17 Z. Wen, W. Zhai, C. Liu, J. Lin, C. Yu, Y. Huang, J. Zhang and C. Tang, *RSC Adv.*, 2019, **9**, 24928–24934.
18 G. Yuan, C. Ritchie, M. Ritter, S. Murphy, D. E. Gómez and P. Mulvaney, *J. Phys. Chem. C*, 2018, **122**, 13407–13415.
19 M. Anaya, A. Rubino, T. C. Rojas, J. F. Galisteo-López, M. E. Calvo and H. Míguez, *Adv. Opt. Mater.*, 2017, **5**, 1601087.
20 W. Wu, C. Zhao, M. Hu, A. Pan, W. Xiong and Y. Chen, *Nanoscale*, 2023, **15**, 5705–5711.
21 W. Nie and H. Tsai, *J. Mater. Chem. A*, 2022, **10**, 19518–19533.
22 M. J. Ashley, M. N. O'Brien, K. R. Hedderick, J. A. Mason, M. B. Ross and C. A. Mirkin, *J. Am. Chem. Soc.*, 2016, **138**, 10096–10099.
23 S. Demchyshyn, J. M. Roemer, H. Groiß, H. Heilbrunner, C. Ulbricht, D. Apaydin, A. Böhm, U. Rütt, F. Bertram, G. Hesser, M. C. Scharber, N. S. Sariciftci, B. Nickel, S. Bauer, E. D. Głowacki and M. Kaltenbrunner, *Sci. Adv.*, 2017, **3**, e1700738.
24 Y. Fu, S. Poddar, B. Ren, Y. Xie, Q. Zhang, D. Zhang, B. Cao, Y. Tang, Y. Ding, X. Qiu, L. Shu, J.-F. Liao, D.-B. Kuang and Z. Fan, *ACS Nano*, 2022, **16**, 8388–8398.
25 Y. B. Cao, D. Zhang, Q. Zhang, X. Qiu, Y. Zhou, S. Poddar, Y. Fu, Y. Zhu, J.-F. Liao, L. Shu, B. Ren, Y. Ding, B. Han, Z. He, D.-B. Kuang, K. Wang, H. Zeng and Z. Fan, *Nat. Commun.*, 2023, **14**, 4611.
26 D. Zhang, Q. Zhang, B. Ren, Y. Zhu, M. Abdellah, Y. Fu, B. Cao, C. Wang, L. Gu, Y. Ding, K.-H. Tsui, S. Fan, S. Poddar, L. Shu, Y. Zhang, D.-B. Kuang, J.-F. Liao, Y. Lu, K. Zheng, Z. He and Z. Fan, *Nat. Photonics*, 2022, **16**, 284–290.
27 S. Liang, M. Zhang, S. He, M. Tian, W. Choi, T. Lian and Z. Lin, *Nat. Synth.*, 2023, **2**, 719–728.
28 R. J. Kashtiban, C. E. Patrick, Q. Ramasse, R. I. Walton and J. Sloan, *Adv. Mater.*, 2023, **35**, 2208575.
29 M. Song, B. Zhao, B. Li, K. Wang, Y. Jiang, G. Jia, X. Zhao, B. Yu, Y. Li and F. Yang, *Nat. Synth.*, 2025, **4**, 1025–1026.
30 M. Zhu, H. Yin, J. Cao, L. Xu, P. Lu, Y. Liu, L. Ding, C. Fan, H. Liu, Y. Zhang, Y. Jin, L.-M. Peng, C. Jin and Z. Zhang, *Adv. Mater.*, 2024, **36**, 2403743.
31 C. Allard, L. Alvarez, J.-L. Bantignies, N. Bendiab, S. Cambré, S. Campidelli, J. A. Fagan, E. Flahaut, B. Flavel, F. Fossard, E. Gaufrès, S. Heeg, J.-S. Lauret, A. Loiseau, J.-B. Marceau, R. Martel, L. Marty, T. Pichler, C. Voisin, S. Reich, A. Setaro, L. Shi and W. Wenseleers, *Chem. Soc. Rev.*, 2024, **53**, 8457–8512.
32 A. Badon, J.-B. Marceau, C. Allard, F. Fossard, A. Loiseau, L. Cognet, E. Flahaut, G. Recher, N. Izard, R. Martel and E. Gaufrès, *Mater. Horiz.*, 2023, **10**, 983–992.
33 C. Allard, L. Schué, F. Fossard, G. Recher, R. Nascimento, E. Flahaut, A. Loiseau, P. Desjardins, R. Martel and E. Gaufrès, *Adv. Mater.*, 2020, **32**, 2001429.
34 J. W. Jordan, A. I. Chernov, G. A. Rance, E. S. Davies, A. E. Lanterna, J. Alves Fernandes, A. Grüneis, Q. Ramasse, G. N. Newton and A. N. Khlobystov, *J. Am. Chem. Soc.*, 2023, **145**, 1206–1215.
35 A. Cadena, Á. Pekker, B. Botka, E. Dodony, Z. Fogarassy, B. Pécz and K. Kamarás, *Phys. Status Solidi RRL*, 2023, **17**, 2200284.
36 T. Tanaka, Y. Sato, M. Aizaki, S. Furusawa, R. Senga, K. Suenaga, T. Endo, Y. Miyata and Y. Nakanishi, *Nano Lett.*, 2025, **25**, 14645–14652.
37 H. Yu, X. Cheng, Y. Wang, Y. Liu, K. Rong, Z. Li, Y. Wan, W. Gong, K. Watanabe, T. Taniguchi, S. Wang, J. Chen, Y. Ye and L. Dai, *ACS Photonics*, 2018, **5**, 4520–4528.
38 A. Marronnier, G. Roma, S. Boyer-Richard, L. Pedesseau, J.-M. Jancu, Y. Bonnassieux, C. Katan, C. C. Stoumpos, M. G. Kanatzidis and J. Even, *ACS Nano*, 2018, **12**, 3477–3486.
39 M. Toplak, G. Birarda, S. Read, C. Sandt, S. M. Rosendahl, L. Vaccari, J. Demšar and F. Borondics, *Synchrotron Radiat. News*, 2017, **30**, 40–45.
40 J. Chen, K. Žídek, P. Chábera, D. Liu, P. Cheng, L. Nuuttila, M. J. Al-Marri, H. Lehtivuori, M. E. Messing, K. Han, K. Zheng and T. Pullerits, *J. Phys. Chem. Lett.*, 2017, **8**, 2316–2321.
41 O. H.-C. Cheng, T. Qiao, M. Sheldon and D. H. Son, *Nanoscale*, 2020, **12**, 13113–13118.
42 G. Rainò, N. Yazdani, S. C. Boehme, M. Kober-Czerny, C. Zhu, F. Krieg, M. D. Rossell, R. Erni, V. Wood, I. Infante and M. V. Kovalenko, *Nat. Commun.*, 2022, **13**, 2587.
43 B. Botka, M. E. Füstös, H. M. Tóháti, K. Németh, G. Klupp, Z. Szekrényes, D. Kocsis, M. Utczás, E. Székely, T. Váczi, G. Tarczay, R. Hackl, T. W. Chamberlain, A. N. Khlobystov and K. Kamarás, *Small*, 2014, **10**, 1369–1378.
44 A. Cadena, B. Botka and K. Kamarás, *Oxford Open Mater. Sci.*, 2021, **1**, itab009.
45 B. T. Diroll, H. Zhou and R. D. Schaller, *Adv. Funct. Mater.*, 2018, **28**, 1800945.
46 H. Yang, T. Cai, L. Dube, K. Hills-Kimball and O. Chen, *Cryst. Growth Des.*, 2021, **21**, 1924–1930.

47 H. M. Tóháti, Á. Pekker, P. Andričević, L. Forró, B. Náfrádi, M. Kollár, E. Horváth and K. Kamarás, *Nanoscale*, 2017, **9**, 17781–17787.
48 V. A. Eremina, T. Eremin, H. Jiang, R. Dhama, J. Odutola, H. Caglayan, N. V. Tkachenko and P. A. Obraztsov, *Adv. Funct. Mater.*, 2025, **2**, 2503397.
49 M. Tomoscheit, J. Schröer, J. S. Virdee, R. Schwartz, C. E. Patrick, R. J. Kashtiban and T. Korn, *Small Sci.*, 2026, **6**, e202500427.
50 Y. Zhou, J. Luo, Y. Zhao, C. Ge, C. Wang, L. Gao, C. Zhang, M. Hu, G. Niu and J. Tang, *Adv. Opt. Mater.*, 2018, **6**, 1800679.
51 K. E. Walker, G. A. Rance, Á. Pekker, H. M. Tóháti, M. W. Fay, R. W. Lodge, C. T. Stoppiello, K. Kamarás and A. N. Khlobystov, *Small Methods*, 2017, **1**, 1700184.
52 S. Cheng and H. Zhong, *J. Phys. Chem. Lett.*, 2022, **13**, 2281–2290.
53 X. Yuan, X. Hou, J. Li, C. Qu, W. Zhang, J. Zhao and H. Li, *Phys. Chem. Chem. Phys.*, 2017, **19**, 8934–8940.
54 J. Liu, K. Song, Y. Shin, X. Liu, J. Chen, K. X. Yao, J. Pan, C. Yang, J. Yin, L.-J. Xu, H. Yang, A. M. El-Zohry, B. Xin, S. Mitra, M. N. Hedhili, I. S. Roqan, O. F. Mohammed, Y. Han and O. M. Bakr, *Chem. Mater.*, 2019, **31**, 6642–6649.
55 A. S. Tutantsev, N. N. Udalova, S. A. Fateev, A. A. Petrov, W. Chengyuan, E. G. Maksimov, E. A. Goodilin and A. B. Tarasov, *J. Phys. Chem. C*, 2020, **124**, 11117–11123.
56 X. Li, Y. Wu, S. Zhang, B. Cai, Y. Gu, J. Song and H. Zeng, *Adv. Funct. Mater.*, 2016, **26**, 2435–2445.
57 D. Hong, Y. Zhang, S. Pan, H. Liu, W. Mao, Z. Lu and Y. Tian, *J. Phys. Chem. Lett.*, 2022, **13**, 10751–10758.
58 B. Akbali, G. Topcu, T. Guner, M. Ozcan, M. M. Demir and H. Sahin, *Phys. Rev. Mater.*, 2018, **2**, 034601.
59 X. Yu, L. Wu, D. Yang, M. Cao, X. Fan, H. Lin, Q. Zhong, Y. Xu and Q. Zhang, *Angew. Chem.*, 2020, **132**, 14635–14640.
60 M. J. Tank, A. N. Reyes, J. G. Park, L. R. Scammell, M. W. Smith, A. De Leon and R. D. Sweat, *ACS Appl. Nano Mater.*, 2022, **5**, 12444–12453.
61 S. Dolati, A. Fereidoon and K. R. Kashyzadeh, *Int. J. Emerging Technol. Adv. Eng.*, 2012, **2**, 470.
62 Y. Yue, X. Yang, K. Yang, K. Li, Z. Liu, F. Wang, R. Zhang, J. Huang, Z. Wang, L. Zhang and G. Xin, *ACS Appl. Mater. Interfaces*, 2024, **16**, 33971–33980.
63 L. Vera-Londono, A. Ruiz-Clavijo, O. Caballero-Calero and M. Martín-González, *Nanoscale Adv.*, 2020, **2**, 4591–4603.
64 T. Coquil, E. K. Richman, N. J. Hutchinson, S. H. Tolbert and L. Pilon, *J. Appl. Phys.*, 2009, **106**, 034910.
65 W. Wenseleers, S. Cambré, J. Čulin, A. Bouwen and E. Goovaerts, *Adv. Mater.*, 2007, **19**, 2274–2278.
66 A. Fitó-Parera, M. Á. López Carrillo, M. E. Tonye, M. Erkens, P. Cool, W. Wenseleers, S. Forel and S. Cambré, *Carbon Trends*, 2025, **18**, 100439.
67 M. D. Özeren, Á. Pekker, K. Kamarás and B. Botka, *RSC Adv.*, 2022, **12**, 28853–28861.
68 C. J. Simonsen Ginestra, C. Martínez-Jiménez, A. Matatyaho Ya'akobi, O. S. Dewey, A. D. Smith McWilliams, R. J. Headrick, J. A. Acapulco, L. R. Scammell, M. W. Smith, D. V. Kosynkin, D. M. Marincel, C. Park, S.-H. Chu, Y. Talmon, A. A. Martí and M. Pasquali, *Nat. Commun.*, 2022, **13**, 3136.
69 V. R. Kode, M. E. Thompson, C. McDonald, J. Weicherding, T. D. Dobrila, P. S. Fodor, C. L. Wirth and G. Ao, *ACS Appl. Nano Mater.*, 2019, **2**, 2099–2105.
70 D. Zhang, Y. Zhu, Q. Zhang, B. Ren, B. Cao, Q. Li, S. Poddar, Y. Zhou, X. Qiu, Z. He and Z. Fan, *Nano Lett.*, 2022, **22**, 3062–3070.
71 S. Matsushita, K. Otsuka, T. Sugihara, G. Zhu, K. Kittipaisalsilpa, M. Lee, R. Xiang, S. Chiashi and S. Maruyama, *ACS Appl. Mater. Interfaces*, 2023, **15**, 10965–10973.